

Characterization of bulk bimodal polycrystalline nickel deformed by direct impact loadings



G. Dirras^{a,*}, D. Tingaud^a, G. Csiszár^b, J. Gubicza^b, H. Couque^c, F. Momprou^d

^a Université Paris 13, Sorbonne Paris Cité, LSPM CNRS, 99 avenue Jean Baptiste Clément, 93430 Villetaneuse, France

^b Department of Materials Physics, Eötvös Loránd University, Budapest, P.O.B. 32, H-1518, Hungary

^c Nexter-Munitions, 7 route de Guerry, 18000 Bourges, France

^d Université Paul Sabatier, CEMES-CNRS, 29 rue Jeanne Marvig, 31055 Toulouse, France

ARTICLE INFO

Article history:

Received 2 January 2014

Accepted 13 February 2014

Available online 20 February 2014

Keywords:

Nickel
Spark plasma sintering
Bimodal microstructure
Impact
Dislocations
Nanohardness

ABSTRACT

Spark plasma sintering of a blend of powders with nanometer and micrometer sized particles yielded to a composite-like nickel microstructure consisting of ultrafine-grained (UFG) and coarse-grained (CG) volumes with the fractions of 36% and 64%, respectively. Microstructure evolution and nanohardness distributions of specimens submitted to impact loading at various velocities between 12 and 50 ms⁻¹ were determined. At a velocity of 12 ms⁻¹, cracks were formed in the UFG regions but they were stopped by the CG entities. Higher velocities resulted in crack-free microstructures and considerable grain fragmentation within CG regions. X-ray line profile analysis investigations showed a decrease of mean crystallite size from ~104 (initial state) to ~41 nm (highest velocity). The dislocation density first increased up to 20 ms⁻¹ then it decreased considerably with increasing impact velocity, indicating recovery in the microstructure due to the conversion of plastic work into heat. Accordingly, the average nanohardness decreased with increasing the velocity from 20 to 31 ms⁻¹. No difference between the microstructures impacted at 31 and 50 ms⁻¹ was observed.

© 2014 Elsevier B.V. All rights reserved.

1. Introduction

Nickel is a widely used structural material in various civilian and military applications due to its high strength even at elevated temperatures. Different methods have been proposed for the preparation of microstructures with improved mechanical properties, including alloying, grain refinement and design of bimodal or multimodal grain structure. Most often, the mechanical properties of these materials are measured under quasi-static conditions. However, due to more and more demanding and complex performances for structural materials, they need to be studied under various loading conditions and environments. Indeed, the increment in strain rate has a crucial impact on the deformation mechanisms and the mechanical properties of conventional materials. In practice, high strain rate deformation occurs during impact loading [1–3] and high speed machining [4–6].

At the macroscopic level, it is generally observed that the flow stress increases with increasing strain rate [7–9]. More precisely, the plot of the flow stress versus the logarithm of strain rate usually displays a steep raise in flow stress at strain rates higher than about 10³ s⁻¹ [10] which is believed to correspond to a transition of deformation mechanism from thermally activated overcoming of

obstacles by dislocations to viscous drag-controlled dislocation motion [11]. Previous studies [1,2] on face centered cubic metals and alloys showed that the deformation at high strain rates is accompanied by an increase in dislocation density. In other studies an increment in ductility during dynamic tensile test [12,13] was reported. Muller [14] used split-Hopkinson pressure bar at strain rates ranging from 500 to 6400 s⁻¹ and investigated the high strain rate response of coarse-grained (CG) nickel (70 μm). The author showed that the flow stress increased and decreased with increasing strain rate and temperature, respectively.

Rajaraman et al. [15] studied the dynamic behavior of microcrystalline and nanocrystalline nickel by compression up to the strain rate of 6450 s⁻¹ using a Kolsky bar. They observed strain softening for nanocrystalline nickel at high strain rates, contrarily to strain hardening behavior in the case of microcrystalline counterparts. In our previous study, high strain rate impact was carried out on CG Ni using a direct impact Hopkinson pressure bar (DIHPB) [3]. The nanohardness of the impacted materials increased with increasing velocity up to 28 ms⁻¹ which was related to the increase of the dislocation density. However, a further increase of the impact velocity to 71 ms⁻¹ resulted in a decrease of hardness back to the value characteristic for the unloaded material. This is a consequence of recovery and recrystallization occurred due to temperature rise during dynamic loading. Additionally, Jonnalagadda [16] reported an increase in twin density in CG nickel with the mean grain size of 32 μm when deformed at high strain rates. Gurao et al. [17] found

* Corresponding author. Tel.: +33 1494 03488; fax: +33 1494 03938.

E-mail address: dirras@univ-paris13.fr (G. Dirras).

an increase in the fraction of high angle grain boundaries (HAGB) at the expense of the low angle grain boundaries (LAGB). They also reported microband formation, grain fragmentation and a decrease of the volume fraction of $\langle 110 \rangle$ oriented grains at high strain rates.

The above discussion shows that the majority of the available data were obtained on mono-modal (CG or nano-grained) materials. However, bi- or multimodal microstructures draw more and more attention as the embedding of coarse grains in the ultrafine-grained (UFG) matrix can offset the inherent lack of ductility of UFG materials. Indeed Lee et al. [18] found that a bimodal Al–7.5 Mg alloy comprising nanocrystalline grains separated by CG regions, shows balanced mechanical properties with enhanced strength and reasonable ductility, as compared to either conventional alloys or UFG counterparts. In addition, tensile and hardness tests suggested unusual deformation mechanisms and interactions between ductile CG bands and nanocrystalline regions. Li et al. [19] compared the high cycle fatigue (HCF) properties of Ti–6Al–2Zr–1Mo–1V alloys with lamellar and bimodal microstructures. Whereas, the difference between the HCF strength values was small for the two microstructures; the lamellae structure provided higher fatigue crack growth resistance than the simple bimodal structure, and the lamellar microstructure displayed a more tortuous and deflected crack path. Zhu and Lu [20] modeled the plastic deformation of nanostructured metals with bimodal grain size distribution, focusing on the behavior of nano- and microcracks. They found that these cracks do not lead to catastrophic failure; instead, they induce additional dislocations, leading to back stresses in the UFG matrix which finally result in strain hardening.

Besides Ni, other metallic materials may also benefit from the evolution of bimodal grain structure. For instance, a powder metallurgy route was used to develop a ferritic steel alloy with bimodal grain size distribution [21]. In this process, the gas-atomized and mechanical alloyed powders blend was sintered by hot forging and the as-consolidated material was annealed. Mechanical tests revealed a great improvement in ductility due to the micron-sized coarse grains in comparison with other ODS ferritic steels, and high strength over the whole range of test temperatures owing to the fine-grained volumes and the oxide nanoparticles. Sitarama Raju et al. [22] demonstrated an approach for retaining high strength while recovering ductility in a Cu–3 at% Ag alloy through cold rolling and short-time annealing. Improvement of uniform elongation to about 10%, as compared to the as-rolled state, was attributed to the development of a bimodal grain structure.

The literature overview presented above shows the potential of bimodal microstructures in improving mechanical performance. Nevertheless, the investigated properties are measured only in quasi-static conditions. However, high speed forming processes necessitate the investigations of the mechanical properties during high strain rate condition at least. Therefore, it is of utmost interest to uncover the high strain rate behavior of such microstructures.

In the present work, DIHPB setup was used to investigate the high strain rate mechanical response of a bimodal nickel consisting of 36% UFG (mean grain size $< 1 \mu\text{m}$) and 64% CG (mean grain size $> 1 \mu\text{m}$) volumes. The microstructure developed during impact test was investigated by EBSD and X-ray diffraction peak profile analysis and transmission electron microscopy. In addition, nanohardness investigations were carried out to scrutinize the local mechanical properties after impact loadings.

2. Experimental materials and procedures

2.1. Sample processing

The starting material was a blend of 40 vol% Ni nanopowder supplied by Tekna (Sherbrooke, Quebec, Canada) and 60 vol% Ni micrometer-sized powder provided by Sigma-Aldrich (St. Louis, MO,

USA). The former powder consisted of spherical particles with the mean size of $\sim 50 \text{ nm}$, while the latter one was made of particle agglomerates having irregular shape and an average size of about $5 \mu\text{m}$ [23]. The **Supplementary material** actually shows the particle size and morphology in the powders. The powders were handled in a glove box under Ar atmosphere. The blending step was carried out for 15 h in a Turbula mixer with helicoidal movement. Afterward, spark plasma sintering (SPS) was used to consolidate the blend of powders. The SPS was carried out using a Syntex 515S machine located at the CNRS platform facility of ICMPE (Thiais, France). The sintering was performed in Ar atmosphere. First, the material was heated up to $500 \text{ }^\circ\text{C}$ at a rate of about $100 \text{ }^\circ\text{C}/\text{min}$, then it was kept at $500 \text{ }^\circ\text{C}$ for 1 min under a pressure of 100 MPa. The consolidation yielded a disk which was about 4 mm in thickness and 20 mm in diameter. The relative density of the sintered disk was $99.4 \pm 0.5\%$, as determined by averaging three measurements obtained by Archimedes' principle. The details of the SPS procedure have been described in [24].

2.2. DIHPB experiments

Impact loadings were conducted on cylindrical specimens with the diameter of 5.9 mm and the height of 3 mm cut from the as-consolidated disk. Four different velocities of 12, 20, 31 and 50 ms^{-1} were applied, which correspond to the initial strain rates of 3700, 6240, 9720 and $15,500 \text{ s}^{-1}$, respectively. No stop ring was used to limit the maximum strain value. Therefore, the strain after impact was different for each velocity as shown in Table 1. The higher the velocity, the larger the maximum strain. More details of the present DIHPB procedure have already been given elsewhere [3].

2.3. Microstructure investigations

A Zeiss Supra 40VP FEG scanning electron microscope was used for EBSD study on the evolution of the microstructure and the local texture. The step size between the neighboring measurement positions was 50 nm. The samples for EBSD investigations were prepared by mechanical grinding using 4000 grit SiC papers, and a finish step was performed using OP-S suspension from Struers. The total duration of the polishing process was about 20 min. The average grain size and the misorientation distribution of grain boundaries were extracted from EBSD scans using an orientation imaging software OIM version 4 from TexSem Laboratories.

In addition to EBSD studies, the microstructure of the initial and the impacted Ni samples was studied by X-ray line profile analysis. The X-ray line profiles were measured by a high-resolution rotating anode diffractometer (type: RA-MultiMax9, manufacturer: Rigaku) using $\text{CuK}\alpha_1$ ($\lambda = 0.15406 \text{ nm}$) radiation. Two-dimensional imaging plates detected the Debye–Scherrer diffraction rings. The line profiles were determined as the intensity distribution perpendicular to the rings obtained by integrating the two dimensional intensity distribution along the rings. The line profiles were evaluated by the extended Convolutional Multiple Whole Profile (eCMWP) analysis [25,26]. In this method, the

Table 1

The mechanical characteristics of the samples impacted at different impact velocities (v) and strains. The temperature rise (ΔT) was evaluated following the Taylor–Quinney approximation. e : Engineering strain, (de/dt) : strain rate, ϵ : true strain, $\sigma_{0.2}$: proof stress at 0.2% plastic strain, T_m : melting point.

v [m/s]	e [%]	(de/dt) [s^{-1}]	ϵ	$\sigma_{0.2}$ [MPa]	ΔT [K]	T [K]	T/T_m
12	56	3700	0.81	876	161	459	0.26
20	76	6240	1.44	960	313	611	0.35
31	82	9720	1.73	1400	549	847	0.48
50	86	15500	1.96	1650	733	1031	0.59

diffraction pattern is fitted by the sum of a background spline and the convolution of the instrumental pattern and the theoretical line profiles related to crystallite size, dislocations and twin faults. The area-weighted mean crystallite size ($\langle x \rangle_{\text{area}}$), the dislocation density (ρ) and the twin boundary probability (β) were determined from the analysis. The area-weighted mean crystallite size was calculated from the median (m) and the variance (σ) of the crystallite size distribution as $\langle x \rangle_{\text{area}} = m \exp(2.5\sigma^2)$. The twin boundary probability corresponds to the relative frequency of twin boundaries among $\{111\}$ lattice planes.

Complementary transmission electron microscopy (TEM) investigations were carried out on the impacted surface of the samples deformed at the lowest and highest velocities of 12 and 50 ms^{-1} , respectively. First, rectangles with the dimensions of 3 mm \times 1 mm \times 0.5 mm were cut from the impacted materials. Then, the specimens were mechanically grinded and thinned by electropolishing using an A2 solution from Struers at -10°C and at a voltage of 20 V. JEOL 2010HC electron microscope operated at 200 kV was used for TEM investigations.

2.4. Nanohardness studies

The local mechanical behavior of the as-consolidated and impacted samples was studied by nanohardness measurements using an UMIS nanoindentation device with Berkovich indenter and applying a maximum load of 2 mN. The loading rate was 0.15 mNs^{-1} . Four hundred indentations were carried out arranging the indents in a 20 \times 20 matrix. The distance between the neighboring indents was 20 μm . The maximum penetration depth was between 70 and 140 nm for all the measurements which corresponds to the indent size between 0.5 and 1 μm . The hardness is characterized by the number determined as [27]

$$H = \frac{P_m}{24.5 h_m^2}$$

where P_m is the maximum load (2 mN) and h_m is the maximum penetration depth during indentation.

3. Results and discussion

3.1. Microstructure of the as-consolidated material

In the present study the UFG and CG components of the microstructure are defined as regions consisting of grains with the size lower and larger than 1 μm , respectively, in accordance with the generally accepted terminology [28,29]. Fig. 1a is a SEM micrograph that gives a general view of the as-processed sample obtained by SPS. The fractions of UFG and CG volumes were 36% and 64%, respectively. Fig. 1b–d shows EBSD images for the as-consolidated material. The color code given by the inset in Fig. 1b indicates that the crystallographic orientation of the grains is random. The microstructure consists of UFG and CG regions as shown in Fig. 1c where the grains with various sizes are indicated by different colors (see the inset). Additionally, many CG single crystals can be seen inside the UFG volumes, which were probably formed by an anomalous grain-growth during SPS processing, as it has been reported in a previous study [29]. The EBSD boundary map shown in Fig. 1d indicates a large fraction ($\sim 26\%$) of $\Sigma 3$ boundaries (denoted by red lines) including coherent twin boundaries. The fractions of the different boundary types according to their misorientation angle are shown in the inset in Fig. 1d. These observations are in accordance with the results of former investigations [3,23].

3.2. Impacted samples

3.2.1. The mechanical behavior at macro-scale

The proof stress at 0.2% plastic strain was calculated from the data recorded during the impact tests. The values of the proof stress determined at different impact velocities are listed in Table 1. Fig. 2 shows the proof stress versus the logarithm of the initial strain rate. The latter quantity was calculated as the ratio of the impact velocity and the initial sample height. In accordance with former observations [10,31,32], the strain rate dependence of the proof stress can be subdivided into two regimes. At low strain rates the proof stress only weakly depends on the strain rate (quasi-static regime), while above 10^3 s^{-1} a steep increment in the proof stress is observed with increasing strain rate (dynamic regime). It has been proposed that in the former regime the deformation is controlled by thermally activated overcoming of glide obstacles by dislocations, while in the latter one viscous drag against dislocation motion operates [33]. Fig. 2 reveals that the proof stress of the bimodal microstructure is higher than that of the conventional coarse-grained material in both quasi-static and dynamic regimes. For low strain rates (quasi-static regime) the proof stress of the bimodal material ($\sim 500 \text{ MPa}$) is about 40% higher than that for the conventional coarse-grained material ($\sim 350 \text{ MPa}$). This difference can be explained by the harder UFG fraction in the bimodal sample. Additionally, X-ray diffraction revealed the existence of crystalline NiO besides the main Ni phase. The ratio of the integrated intensities under the diffraction peaks of NiO and Ni phases was $2.4 \pm 0.3\%$ for the bimodal sample, while peaks of NiO were not detected for the conventional coarse-grained Ni material. Most probably, this oxide phase was originated from the native oxide layer on the surface of the Ni particles in the nanopowder. Therefore, it is suspected that the NiO grains are located in the UFG fraction of the bimodal sample and contribute to the increase of the hardness by dispersion strengthening. The difference between the proof stresses of the bimodal and the conventional materials increases with increasing strain rate in the dynamic regime. As for viscous drag the flow stress is inversely proportional to the mobile dislocation density [30,33]; the much higher stress of the bimodal sample as compared to the coarse-grained material in the dynamic regime may be caused by a smaller mobile dislocation density in the UFG volumes of the bimodal specimen due to the hindering effect of oxide dispersoids and grain boundaries on dislocation motion. It is noted that the lower mobile dislocation density does not necessarily mean a smaller total dislocation density in the UFG region of the as-consolidated material. It should also be noted that in some papers [1,34–36] it is suggested that the plastic deformation at the very high strain rate of 10^4 s^{-1} is still controlled by thermally activated dislocation mechanisms and the upturn of the flow stress is caused by the acceleration of dislocation generation, leading to an abrupt increase of dislocation density which results in a reduced spacing between gliding obstacles.

3.2.2. Microstructure characterization after impact at 12 ms^{-1}

The EBSD images in Fig. 3 illustrate the grain structure in the sample impacted at the lowest velocity of 12 ms^{-1} employed in the present study. The images presented in Fig. 3a–c show the plane normal to the impact direction (hereafter referred to as normal direction and denoted by ND). The variation of the colors inside the coarse grains indicates small crystallographic misorientations (lower than 5°) caused by dislocation patterns formed due to large plastic deformation. The LAGBs with misorientation larger than 5° are indicated by green lines in Fig. 3b, which seem to form preferably in the vicinity of pre-existing HAGBs where dislocations pile up during impact deformation. The fractions of the different

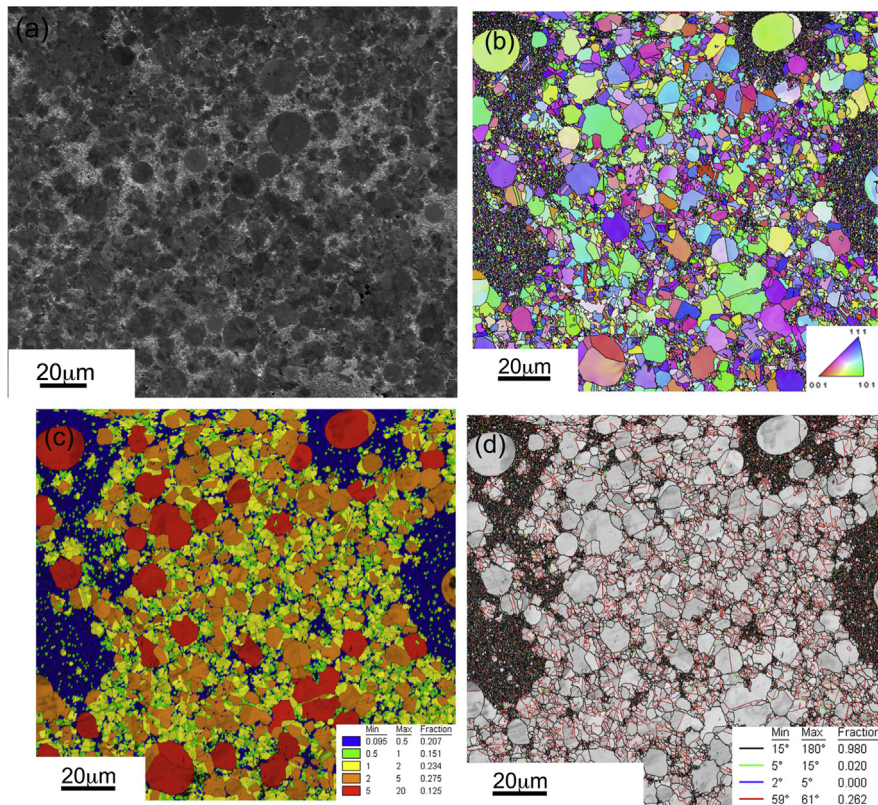


Fig. 1. Microstructure of the as-consolidated sample: (a) overall view by SEM; (b) EBSD inverse pole figure (IPF) where the colors show the crystallographic orientations (the standard triangle is shown in the inset); (c) grain size map (GSM) where the colors are related to different grain size regimes, as indicated in the inset; (d) grain boundary map (GBM) where the different colors denote various misorientation regimes, as shown in the inset. All the images correspond to ND plane. (For interpretation of the references to color in this figure legend, the reader is referred to the web version of this article.)

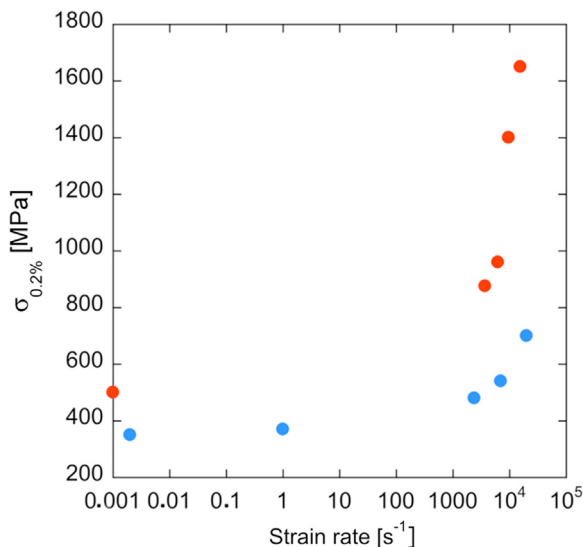


Fig. 2. Plot of the proof stress at 0.2% plastic strain versus the strain rate for bimodal Ni material (red symbols). For comparison, the evolution of the proof stress as a function of strain rate for a conventional Ni with the grain size of $\sim 25 \mu\text{m}$ is also given by blue symbols [10]. (For interpretation of the references to color in this figure legend, the reader is referred to the web version of this article.)

boundary types according to their misorientation angle are shown in the inset in Fig. 3b.

In the UFG component cracks developed but they were stopped at the surrounding CG regions. Most probably, the fast deformation at 12 ms^{-1} caused dislocation motion and multiplication in both UFG and CG volumes. However, in the UFG region the plasticity is hindered by the small grain size and the NiO phase,

therefore microcracks were formed at the grain boundaries, and the crack development was also facilitated by the weaker interface bonding between nanoparticles due to the oxide phase. Fig. 3c illustrates the same behavior when the EBSD investigation was carried out on the surface lying parallel to the impact direction (hereafter referred to as transverse direction and denoted by TD). For both ND and TD views, the larger the area of the UFG component, the longer the cracks.

3.2.3. Microstructure characterization after impact at 20 ms^{-1}

The microstructure of the sample impacted at 20 ms^{-1} is shown in Fig. 4a–d. In the ND view (Fig. 4a) extensive grain fragmentation in the CG volumes can be seen that was accompanied by a tendency to develop a $\langle 220 \rangle$ fiber texture (for the color code see the inset in Fig. 1b and also Section 3.2.4). In addition, the fraction of LAGBs with misorientation angle in the range $5\text{--}10^\circ$ (green lines in Fig. 4b) has increased, as compared to the microstructure after impact at 12 ms^{-1} . Nevertheless, this type of boundary still forms in the vicinity of HAGBs. At the same time, the fraction of $\Sigma 3$ boundaries (red lines in Fig. 4b) became very low and the structure of the UFG volumes could hardly be resolved. It is noted that the decrease of the fraction of $\Sigma 3$ type boundaries has already been reported during quasi-static deformation [23,37], as well as during high strain rate loading [30]. This effect can be related to the interaction between dislocations and twin boundaries during plastic deformation which may yield untwinning [23,38]. The fractions of the different boundary types according to their misorientation angle are shown in the inset in Fig. 4b.

TD views of the microstructure are presented in Fig. 4c and d. The microstructure in these TD views strongly deviates from that

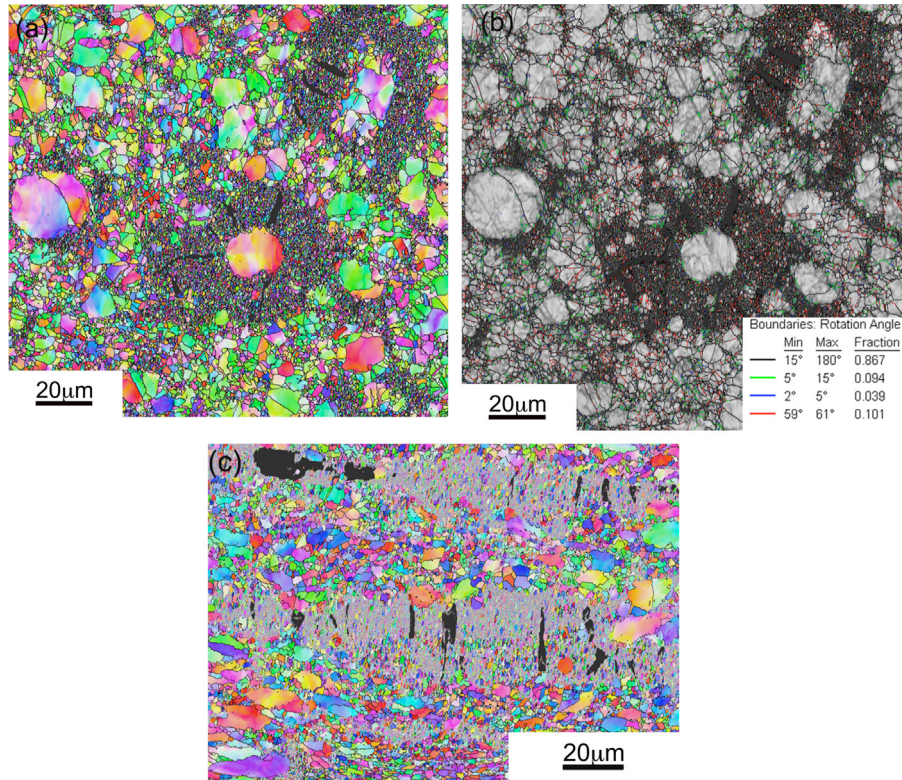


Fig. 3. EBSD micrographs showing the microstructure after impact at the velocity of 12 ms^{-1} : (a) IPF+GBM for ND view, (b) GBM for ND view and (c) IPF for TD view. For the grain orientation in (a) and (c), see the inset in Fig. 1b. (For interpretation of the references to color in this figure, the reader is referred to the web version of this article.)

observed after impact at 12 ms^{-1} . The grains are elongated and flattened, resulting in a lamellar-like structure. The average grain size determined from TD view images is about 241 nm. Localized shear in some elongated coarse grains is also visible, mainly in the vicinity of UFG entities (indicated by thick dashed lines in Fig. 4c). Cracks were hardly observed. Indeed, only a few small spherical holes (indicated by letter H in Fig. 4c) were found, most of them were located at the interfaces between UFG and lamellar CG volumes, probably due to deformation incompatibilities [39].

3.2.4. Microstructure characterization after impact at 31 and 50 ms^{-1}

The microstructures after impact at 31 and 50 ms^{-1} were very similar, therefore only the latter one is discussed here. Fig. 5a shows an EBSD image of the microstructure for the velocity 50 ms^{-1} . The striking feature here is that no cracks or holes were observed, contrarily to the samples impacted at 12 and 20 ms^{-1} . The fractions of the different boundary types according to their misorientation angle are shown in the inset in Fig. 5b.

The microstructure of the UFG component can be investigated in Fig. 5b and c, which indicates that the fraction of UFG component has increased from $\sim 36\%$ to about 50%. This may be caused by an arrangement of dislocations into low angle grain boundaries in the CG volumes due to temperature increase during impact loading at high strains and strain rates, as it has already been reported in former studies [3,30,40]. Additionally, partial recrystallization may also occur which yields small defect-free grains, leading to an increase of the UFG fraction. The structure of the UFG component can now be resolved in the EBSD images (see Fig. 5b and d), contrarily to the case of impact at 20 ms^{-1} (see Fig. 3b), which also suggests a structural relaxation (i.e. recovery) inside the UFG grains.

Actually the temperature rise during impact loading was computed following Taylor and Quinney [41] as

$$\Delta T = \frac{\beta W_p}{\rho_m C_p},$$

where β is the Quinney constant (0.9 was used here assuming that 90% of the plastic work was converted to heat), W_p the plastic strain work per unit mass, ρ_m the mass density (8908 kg m^{-3}) and C_p the specific heat at constant pressure ($446 \text{ J kg}^{-1} \text{ K}^{-1}$). The plastic work per unit mass was obtained from the stress–strain curve determined from the load–displacement data recorded during impact deformation. The temperature rise calculated for different strain rates (and strains) is listed in Table 1. It can be seen that the increment in strain with increasing strain rate results in a considerable temperature rise that could induce recovery processes such as polygonization, as well as partial recrystallization. Indeed, Table 1 shows that the actual temperature in the sample impacted at 50 ms^{-1} is about $0.6 \times T_m$, where T_m is the melting point of Ni. However, Rittel and Osovski [42] pointed out that β depends on both strain and strain-rate and the actual value of about 0.9 might be overestimated. Therefore, the computed temperature rise corresponds to an upper bound. Nevertheless, X-ray line profile analysis and TEM investigations presented in Sections 3.2.5 and 3.2.6, respectively, confirmed recovery processed for the highest impact velocities of 31 and 50 ms^{-1} .

3.2.5. Investigation of the crystallographic texture at a local scale

Fig. 6a and b shows two X-ray diffraction patterns corresponding to the initial sample and the specimen impacted at 20 ms^{-1} , respectively. It can be seen that the intensity of peak 220 became much stronger relative to other reflections due to impact deformation, indicating that in a large fraction of grains the crystallographic direction [220] is lying parallel to the impact direction. Fig. 7 shows the 220 pole figures for the samples impacted at the

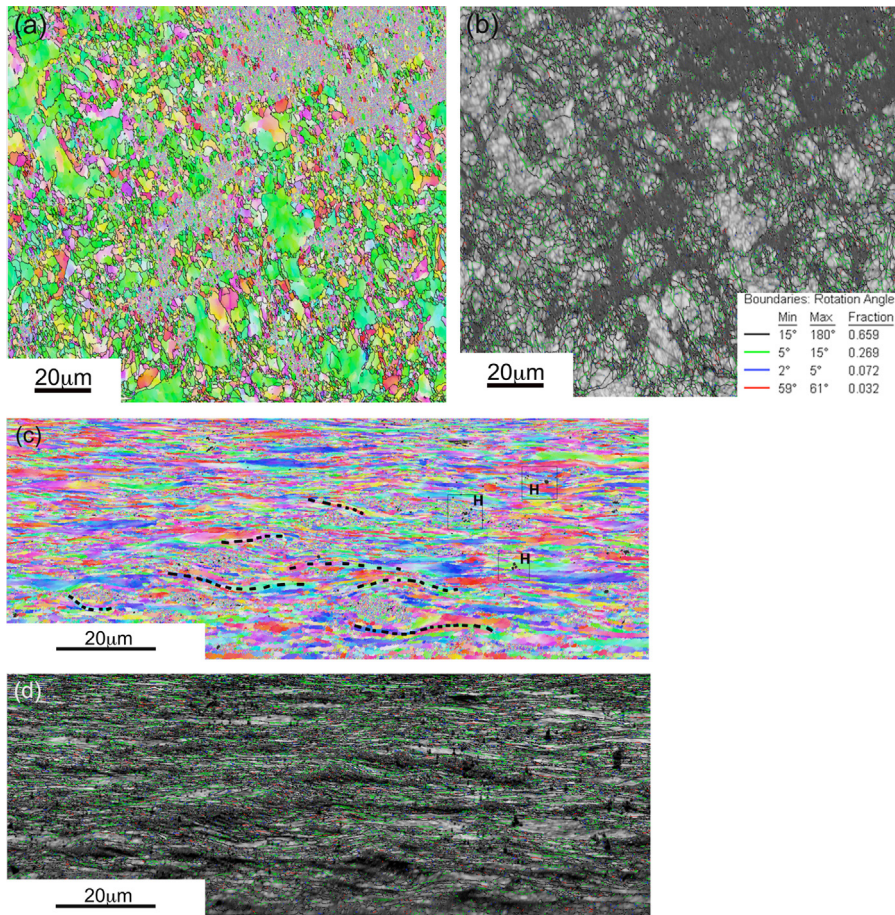


Fig. 4. EBSD micrographs showing the microstructure after impact at the velocity of 20 ms^{-1} : (a) IPF+GBM for ND view, (b) GBM for ND view, (c) IPF for TD view and (d) the corresponding GBM. For the grain orientation in (a) and (c), see the inset in Fig. 1b. See the text for details. (For interpretation of the references to color in this figure, the reader is referred to the web version of this article.)

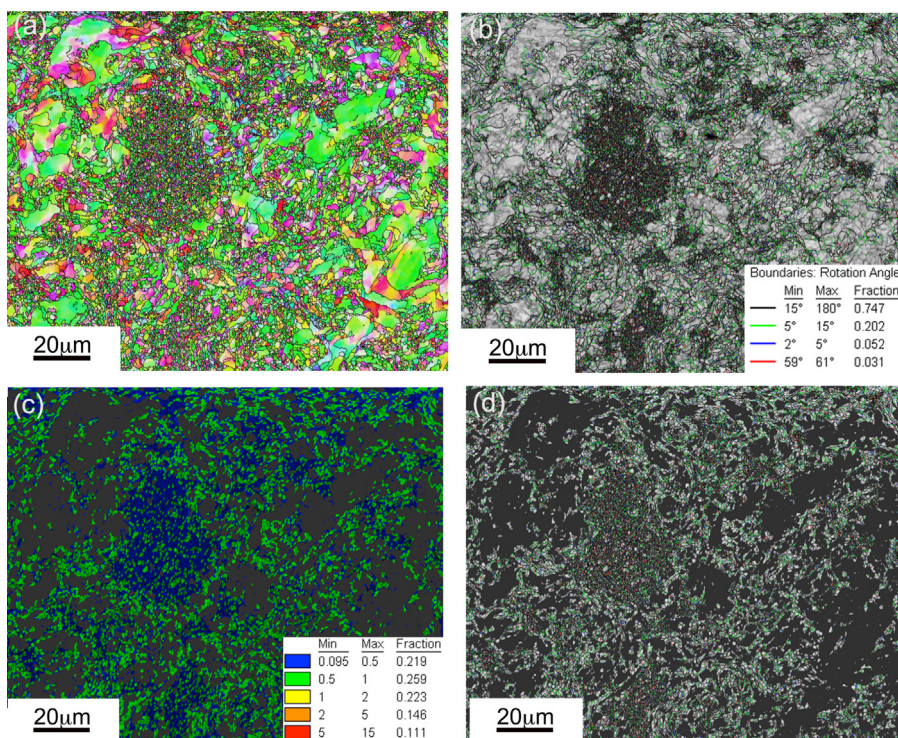


Fig. 5. EBSD micrograph showing the microstructure for ND view after impact at the velocity of 50 ms^{-1} : (a) IPF+GBM, (b) GBM, (c) GSM for the UFG component and (d) the corresponding GBM. For the grain orientation in (a), see the inset in Fig. 1b.

velocities of 12, 20, 31 and 50 ms^{-1} , as extracted from EBSD data. A clear $\langle 220 \rangle$ fiber texture formed whose maximum intensity increased from 1.819 to 3.153 when the velocity increased from 12 to 20 ms^{-1} . The maximum level was almost the same for 20 and 31 ms^{-1} , but it increased to 3.848 after impact at 50 ms^{-1} . However, the fiber is incomplete and shows other deformation components (labeled as A and B) which are well developed

at 50 ms^{-1} , as compared to the case of 31 ms^{-1} but are less intense than for the velocity of 20 ms^{-1} . The evolution of such a $\langle 220 \rangle$ fiber texture during impact of CG Ni has been reported in a previous study [3]. The observed variation of the texture is most probably related to the microstructure re-organization due to grain fragmentation and/or partial recrystallization processes.

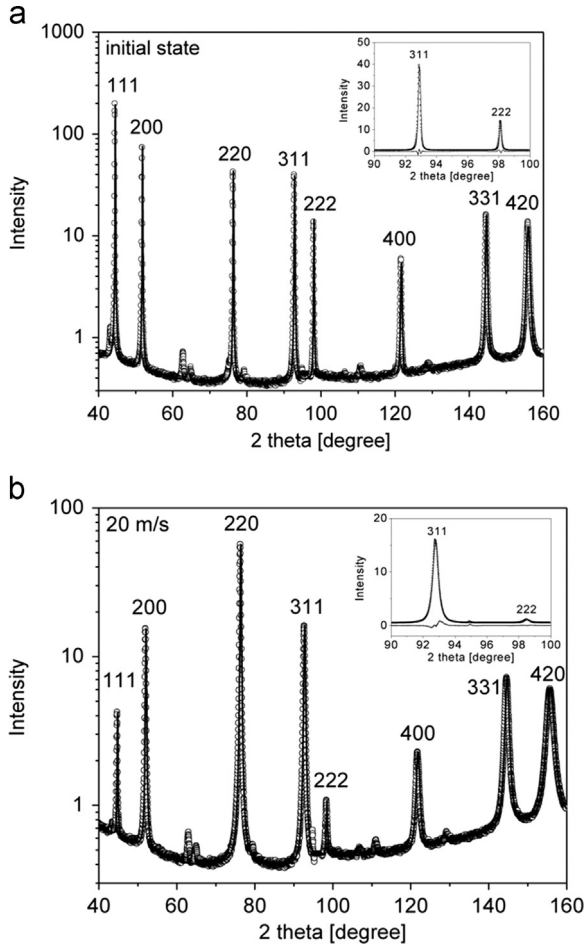


Fig. 6. The eCMWP fitting for (a) the initial as-consolidated Ni sample and (b) the specimen impacted at 20 ms^{-1} . The open circles and the solid line represent the measured data and the fitted curve, respectively. The intensity is plotted in logarithmic scale. The inset shows a part of the pattern in a linear intensity scale. The difference between the measured and the fitted patterns is shown at the bottom of the inset.

3.2.6. Microstructure investigations by X-ray line profile analysis

The microstructure of the initial and the impacted Ni samples was also studied by X-ray line profile analysis. The measured and the fitted patterns for the initial sample and after impactation at 20 ms^{-1} are shown in Fig. 6a and b, respectively. The parameters of the microstructure obtained by X-ray line profile analysis are listed in Table 2. It was found that the crystallite size and the dislocation density considerably decreased and increased, respectively, due to impact deformation at the velocity of 12 ms^{-1} . The crystallite size remained unchanged with the value of about 40–50 nm when the impact velocity (and the associated imposed strain) was further increased. At the same time, the dislocation density decreased considerably when the impact velocity increased from 20 to 31 ms^{-1} . This indicates that above a limiting value of impact velocity the recovery processes are more active which can be explained by the high temperature rise of the sample due to the conversion of plastic work into heat (see above). No difference between the microstructures obtained at 31 and 50 ms^{-1} was observed. The evolution of the twin faults cannot be extracted from X-ray line profile analysis, since the obtained values of the twin boundary probability was very close to the detection limit of this method, $\sim 0.04\%$. This limit corresponds to the twin boundary spacing of ~ 500 nm, if the average spacing of lattice planes is taken as 0.2 nm. In the present materials the average twin boundary spacing is larger than this value, as suggested by the EBSD images shown above.

Table 2

The parameters of the microstructure obtained by X-ray line profile analysis and the mean nanohardness values. $\langle x \rangle_{\text{area}}$ is the area-weighted mean crystallite size, ρ is the dislocation density and β is the twin boundary probability.

Sample	$\langle x \rangle_{\text{area}}$ [nm]	ρ [10^{14}m^{-2}]	β [%]	Nanohardness [GPa]
Initial	104 ± 12	1.4 ± 0.2	< 0.04	8.6
12 ms^{-1}	50 ± 6	25 ± 3	0.04 ± 0.04	8.7
20 ms^{-1}	45 ± 5	18 ± 2	0.10 ± 0.05	10.6
31 ms^{-1}	44 ± 5	7.0 ± 0.8	0.04 ± 0.04	9.6
50 ms^{-1}	41 ± 4	7.2 ± 0.8	< 0.04	9.6

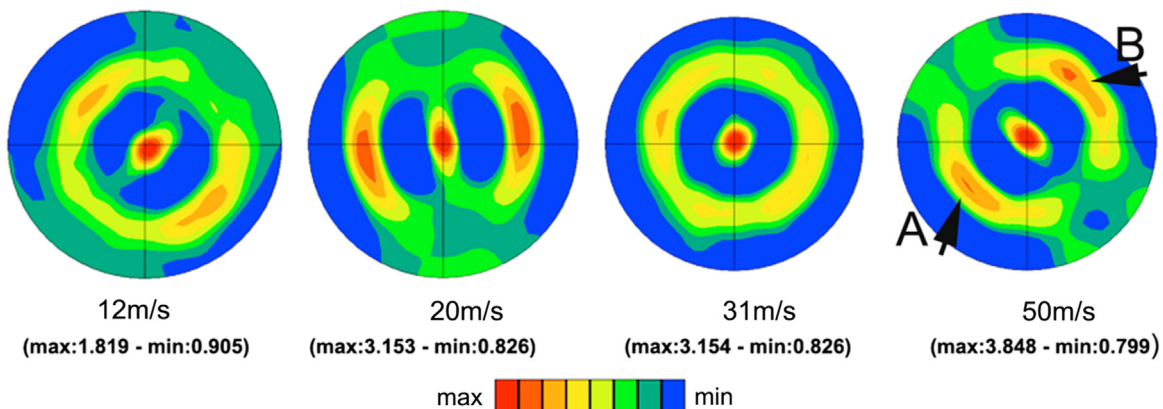


Fig. 7. Illustration of the local crystallographic texture extracted from EBSD investigation and displayed in terms of the $[220]$ pole figures projection on ND plane for the different velocities.

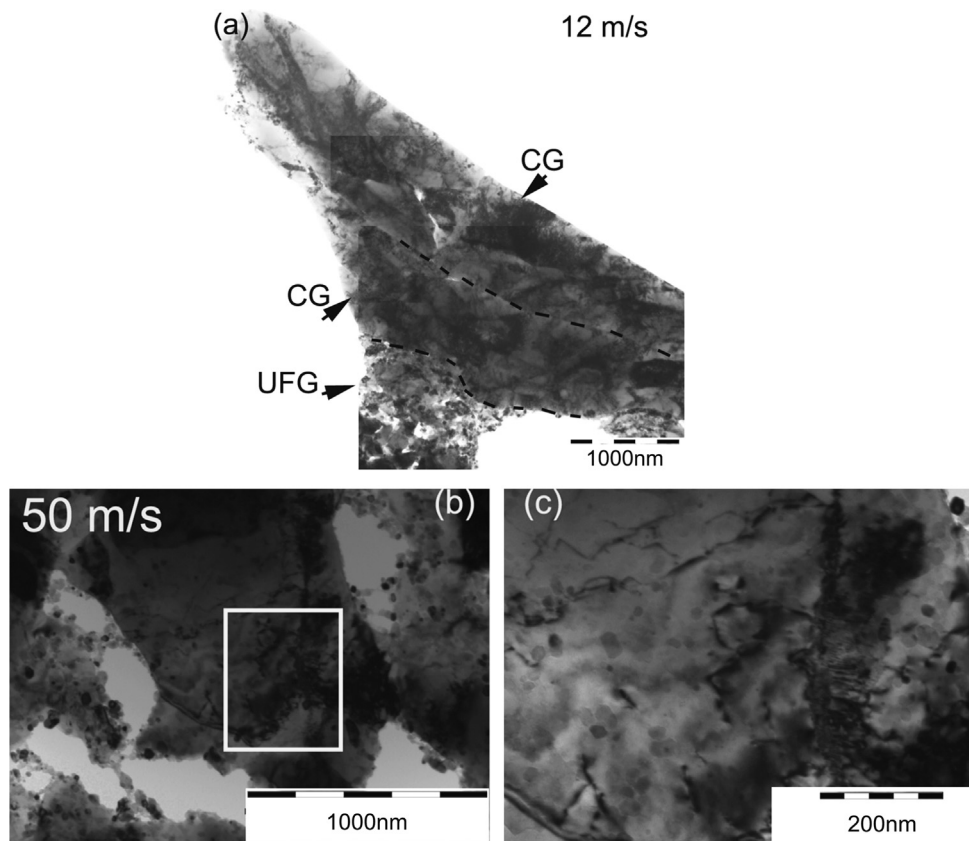


Fig. 8. TEM investigations showing post-mortem microstructures for the samples impacted at (a) 12 and (b) 50 ms^{-1} . Figure (c) is a magnified part of (b).

3.2.7. TEM observations on impacted samples

TEM investigations were performed on the samples impacted at 12 and 50 ms^{-1} which have typical microstructures for low and high velocities, respectively. The TEM image in Fig. 8a obtained after impact deformation at 12 ms^{-1} shows highly elongated grains (the grain boundaries are indicated by dashed lines) with high density of dislocations which form tangles or are arranged into subgrain boundaries. An UFG region can be seen at the left bottom of the figure. Numerous dislocations-free spherical nanocrystals are also found indicating an incomplete sintering within the UFG volume. The weak particle bonding in such regions may contribute to an easier crack nucleation and growth during impact loading as described in Section 3.2.1. Fig. 8b shows a typical microstructure after impact at 50 ms^{-1} . The striking feature is the lower dislocation density in comparison to the sample impacted at 12 ms^{-1} . Additionally, dense subgrain boundaries are observed in Fig. 8c (a magnified part in Fig. 8b), indicating the rearrangement of dislocations during the deformation. These observations are in line with X-ray line profile analysis and EBSD results and support the conclusion that considerable recovery occurs at high impact velocities in accordance with previous studies [3,30].

3.2.8. Study of the local mechanical behavior by nanoindentation

The nanohardness distributions obtained for the as-consolidated and the impacted samples are shown in Fig. 9. The average nanohardness values are also listed in Table 2. In the case of the initial sample there is a bimodal hardness distribution which is in accordance with the bimodal nature of the as-consolidated microstructure. Most probably, the softer and the harder regions correspond to CG and UFG volumes, respectively. Significant changes in the nanohardness distribution were observed due to impact deformation. Despite the change of the distribution, the average hardness after impact at 12 ms^{-1} is practically the same as for the initial sample before

deformation. This can be attributed to the softening effect of the cracks in the UFG component (see Fig. 3), which can compensate the hardening caused by the increase of the dislocation density (see Table 2). This observation is in line with the fact that the second hardness peak present in the initial state (corresponding to the UFG volume as discussed above) has now almost disappeared. After impact at 20 ms^{-1} , the mean nanohardness increased in accordance with the increase of the dislocation density and the reduction of the crystallite size (see Table 2). However, it is interesting that the soft regions in the initial state become harder, while the formerly harder regions become softer, keeping the bimodal nature of the distribution. For this sample EBSD investigations showed that the UFG volumes were less damaged (see Fig. 4) in comparison with the specimen impacted at 12 ms^{-1} . This may indicate a slight recovery in the UFG region due to annealing during impact test. However, the smaller hardness in the UFG region might be also caused by the texture formed due to deformation, as the Schmid factor for a [220] oriented sample (about 2.5) is smaller than that for randomly oriented case (about 3) [43]. At 31 ms^{-1} the fraction of the harder regions decreased, suggesting that the recovery observed by X-ray line profile analysis has occurred mainly in the harder UFG regions. In addition, the mean hardness at 31 ms^{-1} was also reduced, as compared to that obtained for 20 ms^{-1} in accordance with the decrease in the total dislocation density. There is no significant difference between the hardness distributions obtained for 31 and 50 ms^{-1} , which is in line with the microstructure observations.

4. Conclusions

Bulk Ni with bimodal grain structure consisting of UFG and CG regions was consolidated from nanosized and coarse-grained powders by SPS. The evolution of the microstructure during impact

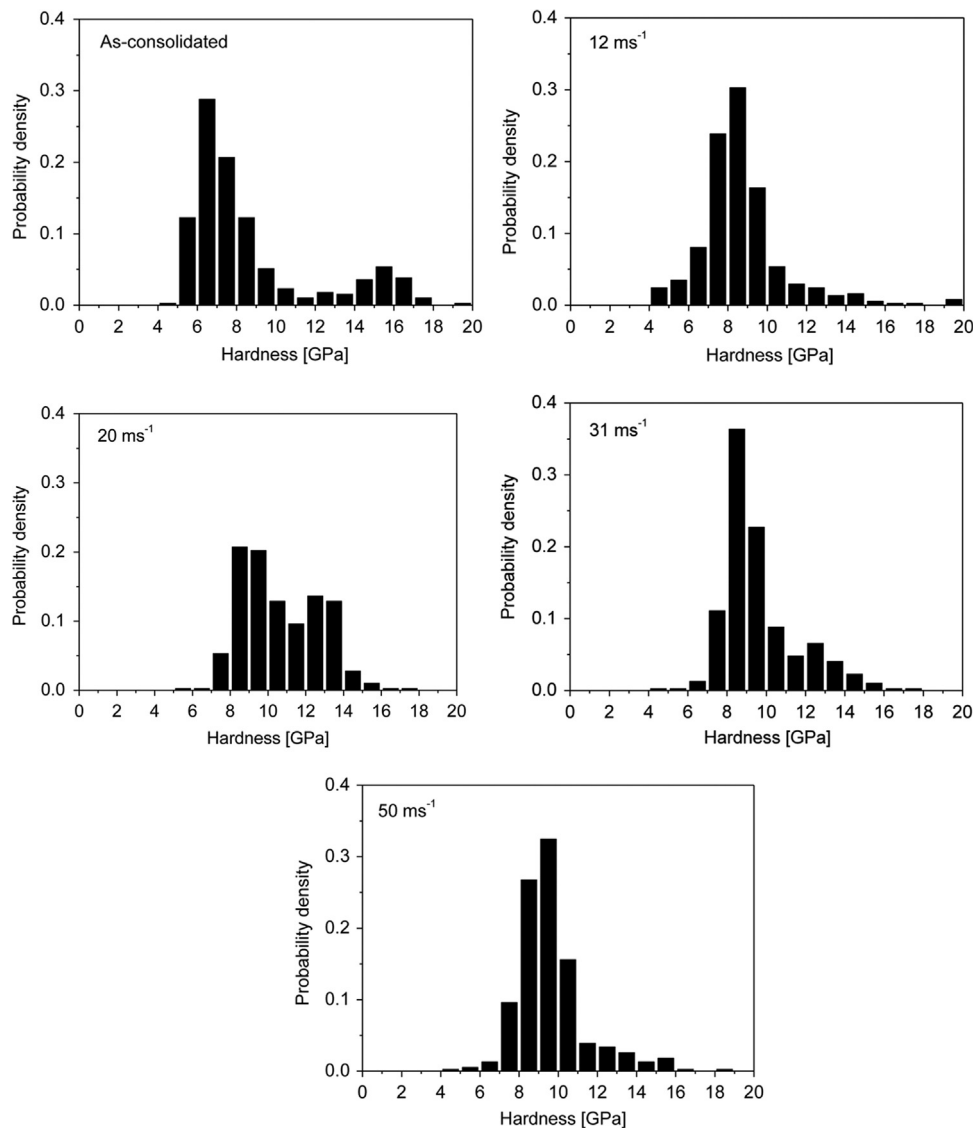


Fig. 9. Nanohardness distributions for the as-consolidated and the impacted samples at different velocities.

deformation at the velocities of 12, 20, 31 and 50 ms⁻¹ has been investigated. The following results were obtained.

- (1) During impact at 12 ms⁻¹ the total dislocation density significantly increased while the grains in the CG volumes were fragmented. Simultaneously, microcracks were developed in the UFG regions which were stopped at CG volumes. Most probably, these cracks were formed due to the hindered plasticity and the incomplete particle bonding in the UFG volumes. The average nanohardness of this sample was practically the same as for the initial material, as the hardening effect of the larger dislocation density was compensated by the softening effect of the cracks.
- (2) For the velocity of 20 ms⁻¹ the average nanohardness was higher than in the case of sample impacted at 12 ms⁻¹, since the dislocation density was high while cracks were not formed. However, the hardnesses of the CG and UFG regions increased and decreased, respectively, as compared to the initial state. The latter effect can be explained by a moderate recovery due to the conversion of plastic work into heat, as well as by the development of a [220] texture.
- (3) The dislocation density and the nanohardness were the same for 31 and 50 ms⁻¹, however, they were lower than

in the case of 20 ms⁻¹. This might be caused by a stronger recovery of the microstructure as it is suggested by the EBSD and TEM investigations, as well as by the nanohardness distribution. This recovery is caused by a larger temperature rise due to heat evolution during high strain rate impact tests.

Acknowledgments

This work was carried out in the framework of the “MIMIC” project funded by the French National Research Agency, ANR-09-BLAN-0010. This work was supported in part by the Hungarian Scientific Research Fund, OTKA, Grant no. K-109021. The authors are grateful to Mr. Péter Szommer for performing nanohardness measurements and to Ms. A. Krawczynska for TEM investigations.

Appendix A. Supporting information

Supplementary data associated with this article can be found in the online version at <http://dx.doi.org/10.1016/j.msea.2014.02.043>.

References

- [1] F.J. Zerilli, R.W. Armstrong, *Acta Metall.* 40 (1992) 1803–1808.
- [2] W.S. Lee, C.F. Lin, *Metall. Mater. Trans. A* 33 (2002) 2801–2810.
- [3] G. Dirras, H. Couque, J. Gubicza, A. Abdelouhab, T. Chauveau, P. Jenei, *Mater. Sci. Eng. A* 527 (2010) 4128–4135.
- [4] N.A. Abukhshim, P.T. Mativenga, M.A. Sheikh, *Int. J. Mach. Tools Manuf.* 46 (2006) 782–800.
- [5] A. Molinari, C. Musquar, G. Sutter, *Int. J. Plasticity* 18 (2002) 443–459.
- [6] T.J. Burns, M.A. Davies, *Int. J. Plasticity* 18 (2002) 487–506.
- [7] X. Wei, F. Renyu, L. Li, *Mater. Sci. Eng. A* 465 (2007) 260–266.
- [8] M. Guden, I.W. Hall, *Comput. Struct.* 76 (2000) 139–144.
- [9] A.G. Odeshi, S. Al-ameeri, M.N. Bassim, *J. Mater. Process. Technol.* 162–163 (2005) 385–391.
- [10] H. Couque, R. Boulanger, in: F. Gálves, V. Sanchez-Galves (Eds.), *Proceedings of the 23rd International Symposium on Ballistics*, Tarragona, Spain, 2007, pp. 255–262.
- [11] A. Kumar, F.E. Hauser, J.E. Dorn, *Acta Metall.* 9 (1968) 1189–1197.
- [12] V.S. Balanethiram, G.S. Daehn, *Scr. Metall. Mater.* 30 (1994) 515–520.
- [13] V.S. Balanethiram, X.Y. Hu, G.S. Daehn, *J. Mater. Process. Technol.* 45 (1994) 595–600.
- [14] T. Muller, *J. Mech. Eng. Sci.* 14 (1972) 161–167.
- [15] S. Rajaraman, Krishna N. Jonnalagadda, P. Ghosh, in V. Chalivendra, B. Song, D. Casem (Eds.), *Dynamic behavior of materials*, Conference Proceedings of the Society for Experimental Mechanics Series 1, 2013, pp. 157–163.
- [16] K. Jonnalagadda, *Conf. Proc. Soc. Exp. Mech. Ser.* 99 (2011) 439–442.
- [17] N.P. Gurao, R. Kapoor, S. Suwas, *Metall. Mater. Trans. A* 41 (2010) 2794–2804.
- [18] Z. Lee, D.B. Witkin, V. Radmilovic, E.J. Lavernia, S.R. Nutt, *Mater. Sci. Eng. A* 410–411 (2005) 462–467.
- [19] S. Li, B. Xiong, S. Hui, W. Ye, Y. Yu, *Mater. Sci. Eng. A* 460–461 (2007) 140–145.
- [20] L. Zhu, J. Lu, *Int. J. Plasticity* 30–31 (2012) 166–184.
- [21] Z. Dapeng, L. Yong, L. Feng, W. Yuren, Z. Liujie, D. Yuhai, *Mater. Lett.* 65 (2011) 1672–1674.
- [22] K. Sitarama Raju, V. Subramanya Sarma, A. Kauffmann, Z. Hegedűs, J. Gubicza, M. Peterlechner, J. Freudenberger, G. Wilde, *Acta Mater.* 61 (2013) 228–238.
- [23] G.-D. Dutel, P. Langlois, D. Tingaud, G. Dirras, *Mater. Charact.* 79 (2013) 76–83.
- [24] G.-D. Dutel, D. Tingaud, P. Langlois, G. Dirras, *J. Mater. Sci.* 47 (2012) 7926–7931.
- [25] G. Ribárik, J. Gubicza, T. Ungár, *Mater. Sci. Eng. A* 387–389 (2004) 343–347.
- [26] L. Balogh, G. Ribárik, T. Ungár, *J. Appl. Phys.* 100 (2006) 023512.
- [27] F. Fröhlich, P. Grau, W. Grellmann, *Phys. Status Solidi* 42 (1977) 79–89.
- [28] S. Cheng, J.A. Spencer, W.W. Milligan, *Acta Mater.* 51 (2003) 4505–4518.
- [29] H. Conrad, *Mater. Sci. Eng. A* 341 (2003) 216–228.
- [30] G. Dirras, A. Ouarem, H. Couque, J. Gubicza, P. Szommer, O. Brinza, *Mater. Charact.* 62 (2011) 480–487.
- [31] H. Zhang, K.T. Ramesh, E.S.C. Chin, *Mater. Sci. Eng. A* 384 (2004) 26–34.
- [32] A. Rusinek, J.A. Rodríguez-Martínez, A. Arias, *Int. J. Mech. Sci.* 52 (2010) 120–135.
- [33] H.J. Frost, M.F. Ashby, *Deformation-Mechanism Maps* Pergamon Press, Oxford, 1982.
- [34] P.S. Follansbee, U.F. Kocks, *Acta Metall.* 36 (1988) 81–93.
- [35] S. Nemat-Nasser, Y. Li, *Acta Mater.* 46 (1998) 565–577.
- [36] A. Molinari, G. Ravichandran, *Mech. Mater.* 37 (2005) 737–752.
- [37] H.Q. Bui, G. Dirras, S. Ramtani, J. Gubicza, *Mater. Sci. Eng. A* 527 (2010) 3227–3235.
- [38] J. Gubicza, *Defect Structure in Nanomaterials*, Woodhead Publishing Cambridge, UK, 2012.
- [39] G. Dirras, J. Gubicza, S. Ramtani, H. Bui, T. Szilágyi, *Mater. Sci. Eng. A* 527 (2010) 1206–1214.
- [40] L. Tang, Z. Chen, C. Zhan, X. Yang, Ch. Liu, H. Cai, *Mater. Charact.* 64 (2012) 21–26.
- [41] G.I. Taylor, H. Quinney, *Proc. R. Soc. Lond.* 143 (1934) 307–326.
- [42] D. Rittel, S. Osovski, *Int. J. Fract.* 162 (2010) 177–185.
- [43] B. Clausen, T. Lorentzen, T. Leffers, *Acta Mater.* 46 (1998) 3087–3098.